Nonlinear development of inertial instability in a barotropic shear

Riwal Plougonven[1,a] and Vladimir Zeitlin[2]
[1]*Laboratoire de Météorologie Dynamique, ENS, IPSL, 24 rue Lhomond, 75005 Paris, France*
[2]*Laboratoire de Météorologie Dynamique, UPMC, IPSL, 24 rue Lhomond, 75005 Paris, France*

(Received 10 June 2009; accepted 10 September 2009; published online 9 October 2009)

Inertial instability is investigated numerically in a two-dimensional setting in order to understand its nonlinear stage and saturation. To focus on fundamental mechanisms, a simple barotropic shear $U(y)=\tanh y$ on the f-plane is considered. The linear stability problem is first solved analytically, and the analytical solutions are used to benchmark numerical simulations. A simple scenario of the nonlinear development of the most unstable mode was recurrently observed in the case of substantial diffusivity: while reaching finite amplitude the unstable mode spreads laterally, distorting the initially vertical instability zone. This process produces strong vertical gradients which are subsequently annihilated by diffusion, making the flow barotropic again but with the shear spread over a wider region. In the course of such evolution, unexpectedly, strong negative absolute vorticity anomalies are produced. In weakly diffusive simulations, the horizontal spreading of the unstable motions and the enhancement of the anticyclonic vorticity extremum persist, but small-scale motions/instabilities render the flow considerably more complex. It is known that the barotropic component of the final state can be predicted from the conservation of momentum. Our simulations confirm the relevance of this simple prediction in the cases investigated regardless of resolution and diffusion. The baroclinic component of the final state is also analyzed and three types of structures are identified: persistent stationary stratification layers, subinertial waves trapped in the anticyclonic shear, and freely propagating inertia-gravity waves. The subinertial waves and the stratification staircase have clear signatures and can therefore help to identify the regions that have undergone inertial instability. © *2009 American Institute of Physics*. [doi:10.1063/1.3242283]

I. INTRODUCTION

Symmetric instability occurs in rotating fluids when the potential vorticity (PV) is of opposite sign to the Coriolis parameter[1] and is the geophysical analog of centrifugal, or Taylor–Couette, instability. Inertial instability is the special case when the relative vorticity is stronger than $-f$ in a certain region of the flow, where f is the (local) Coriolis parameter.[2] It occurs in the atmosphere and oceans in the vicinity of the equator due to either meridional shear[3,4] or interhemisphere advection[5] or due to diabatic processes modifying the PV.[2] Occurrences of inertial instability due to advection can be found at significant distances from the equator.[6,7]

Linear aspects of inertial instability were extensively studied for zonally symmetric flows,[4,8–11] flows with zonal variations,[12,13] and oscillating flows at the equator.[14] For zonally symmetric flows in an inviscid fluid, linear theory shows that the growth rates monotonically increase for increasing vertical wavenumber. However, vertical wavelengths found in observations, for instance, in the equatorial stratosphere and mesosphere at solstice, are not consistent with theoretical predictions based solely on molecular diffusion, making it necessary to understand the nonlinear stage of the instability in order to explain the vertical scale selection.[15] It has been hypothesized that Kelvin–Helmholtz (KH) instabilities inhibiting modes with smaller vertical scales play a role, and this has been tested convincingly with simulations relevant to the equatorial middle atmosphere.[16] In a different configuration the role of KH instabilities in the equilibration of symmetric instability has also been highlighted by numerical simulations in the oceanic context.[17]

In the diffusive regime, the nonlinear behavior of inertial instability has been described in depth via analytical and numerical approaches for a uniform shear near the equator.[15] In the weakly nonlinear regime, it was found that the most unstable mode would grow to a finite amplitude, induce persistent mean-flow changes sufficient to neutralize the flow (homogenization of fQ to a small, negative value, with Q the PV), and then decay. As nonlinearity increases, the overturning cells extend poleward, mixing angular momentum and homogenizing fQ over a wider region. It had been noticed previously[18] for an unstratified flow on the f-plane that a latitudinally narrow mode of inertial instability could, through its nonlinear development, homogenize a latitudinally wide region. A similar behavior has also been documented for axisymmetric flows: numerical simulations of inertial instability in barotropic vortices have shown the formation of dipoles that move horizontally and mix angular momentum throughout a larger region than the initially unstable one.[19]

Regarding the end state of evolution of the inertial instability, it has been shown recently that it can be predicted from simple momentum conservation considerations, in what concerns its barotropic component.[20] The argument is similar to that for geostrophic adjustment of a barotropic jet,[21,22]

[a]Electronic mail: riwal.plougonven@polytechnique.org.

 © 2009 American Institute of Physics

Downloaded 14 Oct 2009 to 129.199.72.169. Redistribution subject to AIP license or copyright; see http://pof.aip.org/pof/copyright.jsp

with the notable difference that PV is not conserved for fluid parcels where it is initially negative. Several questions arise regarding the relevance of this prediction, as well as its sensitivity to the parameters of the numerical simulations, such as resolution and viscosity.

Although the end state does not consist only of the barotropic component, the baroclinic component has received little attention up to now. The construction of the vertically averaged state turns out to be quite simple, yet some developed structures with fine vertical scales may persist. Thorpe and Rotunno,[23] in their numerical investigation of the nonlinear development of symmetric instability, noted that the instability drives the flow toward a state in which regions of negative PV may still exist but are broken down to small, fragmented patches, each having insufficient spatial extent for instability to develop (at least at the resolution used). Hence several questions arise regarding the end state of evolution of the inertial instability: What type of baroclinic motions persist and how intense are they? How sensitive to dissipation and resolution are they? Can they give a clear signature of the former presence of inertial instability?

For flows with strong shears, it should be kept in mind that barotropic instability may compete with inertial instability.[18,20] Inertial instability will nevertheless have the dominant growth rates for the flows considered here (see Ref. 11, Sec. IV), and hence the possibility of barotropic instability will not be investigated.

The object of the present study is to investigate the nonlinear development of inertial instability, with emphasis on the details of nonlinear saturation and its persistent signatures. Our strategy consists in choosing a configuration simple enough to be analytically solved in the linear approximation. The explicitly known unstable mode will allow us to benchmark the numerical model at the initial growth stage, allowing thus for neat investigation of the nonlinear stage.

The paper is organized as follows: The linear stability problem is solved for a barotropic shear layer in Sec. II. The numerical simulations of inertial instability are described and benchmarked in Sec. III. The nonlinear evolution and saturation of the instability are presented in Sec. IV. The question of the final state is addressed in Sec. V, and conclusions are presented in Sec. VI.

II. ANALYTICAL SOLUTIONS OF THE LINEAR STABILITY PROBLEM

A motivation for considering a barotropic shear on the f-plane is the possibility to solve analytically the linear stability problem. The equations of motion are introduced and scaled in Sec. II A, and the linear stability problem is solved in Sec. II B. The growth rates and structures of the unstable modes are described in Sec. II C.

A. General form of the eigenvalue problem

Following Ref. 16 we start from the primitive equations in the Boussinesq approximation and including only the vertical diffusion, with the tildes $\tilde{}$ denoting dimensional variables:

$$\frac{D\tilde{\mathbf{u}}_H}{D\tilde{t}} + \mathbf{f}\times\tilde{\mathbf{u}}_H + \nabla_H\tilde{\phi}_{\rm tot} = \nu\frac{\partial^2\tilde{\mathbf{u}}_H}{\partial\tilde{z}^2}, \tag{1a}$$

$$\frac{D\tilde{w}}{D\tilde{t}} + \frac{\partial\tilde{\phi}_{\rm tot}}{\partial\tilde{z}} - g\frac{\tilde{\theta}_{\rm tot}}{\theta_r} = \nu\frac{\partial^2\tilde{w}}{\partial\tilde{z}^2}, \tag{1b}$$

$$\frac{D\tilde{\theta}_{\rm tot}}{D\tilde{t}} = \kappa\frac{\partial^2\tilde{\theta}_{\rm tot}}{\partial\tilde{z}^2}, \tag{1c}$$

$$\nabla_H\tilde{\mathbf{u}}_H + \frac{\partial\tilde{w}}{\partial\tilde{z}} = 0. \tag{1d}$$

Here $\tilde{\mathbf{u}}_H$ is the horizontal velocity, $D/D\tilde{t}=\partial_{\tilde{t}}+\tilde{\mathbf{u}}\cdot\nabla$ is the full Lagrangian derivative, $\mathbf{f}=f\mathbf{k}$ is the Coriolis parameter times the unit vertical vector, $\tilde{w}$ is the vertical velocity, and ν and κ are the vertical (turbulent) viscosity and diffusivity, respectively. In the atmospheric context, $\tilde{\phi}_{\rm tot}$ is the total geopotential, $\tilde{\theta}_{\rm tot}$ is the total potential temperature, g is the gravity, and $\tilde{\theta}_r$ is a reference potential temperature. The vertical coordinate is the modified pressure coordinate introduced in Ref. 24 and for shallow layers it differs only slightly from geometric height. In the oceanic context, $\tilde{z}$ is the geometric height, $\tilde{\phi}_{\rm tot}$ is $\tilde{P}/\tilde{\rho}_0$, and $\tilde{\theta}$ is the density. In what follows we will consider $f>0$, and negative PV will correspond to inertially unstable regions. Finally, we suppose that the smallest scales occur in the vertical direction; that is why only vertical diffusion is included.

We restrict our attention to flows that are symmetric in $\tilde{x}$: $\partial_{\tilde{x}}\equiv 0$. From the incompressibility constraint (1d) we can then introduce a streamfunction $\tilde{\psi}$ such that $\tilde{v}=-\partial_{\tilde{z}}\tilde{\psi}$ and $\tilde{w}=\partial_{\tilde{y}}\tilde{\psi}$. The potential temperature is split into a background one that varies only in the vertical and a perturbation: $\tilde{\theta}_{\rm tot}(\tilde{y},\tilde{z})=\tilde{\Theta}(\tilde{z})+\tilde{\theta}(\tilde{y},\tilde{z})$. For simplicity we will assume that $N^2=g/\theta_r(d\tilde{\Theta}/dz)$ is constant and that the Prandtl number is unity, i.e., $\kappa=\nu$. We also introduce the notation $\tilde{\chi}=g\tilde{\theta}/\tilde{\theta}_r$.

We now proceed to scale the equations in order to analyze the instability of barotropic shear regions. The shear flow $U\tanh(\tilde{y}/L)$ provides a natural horizontal length scale L and velocity scale U. As the basic flow contains no vertical length scale, it is natural to choose H such that the Burger number $N^2H^2/f^2L^2=1$. In the equations for the nondimensional (no-tilde) variables (u,ψ,ϕ,χ), three parameters appear:

- $\mathcal{R}=U/fL$, the Rossby number, which measures the intensity of the shear relative to planetary vorticity. It appears in the Lagrangian derivative $D=\partial_t+\mathcal{R}(\partial_y\psi\partial_z-\partial_z\psi\partial_y)$.
- $\gamma=\nu/fH^2$, the "Ekman" number, which measures the importance of diffusion relative to rotation. Because inertial instability develops at the smallest available vertical scales in the inviscid fluid, diffusion will in fact be important even for small values of $\gamma=\nu/fH^2$. Note that the Reynolds number is obtained as $\mathrm{Re}=\mathcal{R}/\gamma$.
- $\delta=H/L$, the aspect ratio. As the Burger number is

Downloaded 14 Oct 2009 to 129.199.72.169. Redistribution subject to AIP license or copyright; see http://pof.aip.org/pof/copyright.jsp

unity, we also have $\delta=f/N$. For atmospheric and oceanic flows one has $\delta \ll 1$, and so the hydrostatic approximation ($\delta \to 0$) is justified.

In the case of the inviscid fluid ($\gamma=0$) it is well known (e.g., Ref. 24) that zonally symmetric flows ($\partial_x \equiv 0$) have two Lagrangian invariants: geostrophic momentum and potential temperature. The PV may be expressed in terms of them. The nondimensional expressions of the invariants are, respectively,

$$M = u - \mathcal{R}^{-1} y \quad \text{and} \quad \Theta = \chi + \mathcal{R}^{-1} z. \tag{2}$$

Now, we consider a background barotropic flow that is in geostrophic equilibrium, $U(y)=-\partial_y \Phi_b$, and hence is a stationary solution of the equations. Linearizing about this flow ($u=U+u'$, $\phi=\Phi_b+\phi'$, $\chi=\chi'$, $\psi=\psi'$), the following equations are obtained:

$$\mathcal{D}u' + (1 - \mathcal{R}U_y)\psi_z = 0, \tag{3a}$$

$$\mathcal{D}\psi_z - u' - \phi'_y = 0, \tag{3b}$$

$$\delta^2 \mathcal{D}\psi_y - \chi + \phi'_z = 0, \tag{3c}$$

$$\mathcal{D}\chi + \psi_y = 0, \tag{3d}$$

where $\mathcal{D} \equiv (\partial_t - \gamma \partial_{zz})$ and subscripts denote partial derivatives.

Looking for normal mode solutions of the form $\psi(y,z,t)=\hat{\psi}(y)e^{i(mz-\omega t)}$ and combining the equations in Eq. (2) following standard manipulations, a single equation for $\hat{\psi}(y)$ is obtained:

$$\hat{\psi}_{yy} + \frac{m^2}{1-\hat{\omega}^2\delta^2}[\hat{\omega}^2 - (1 - \mathcal{R}U_y)]\hat{\psi} = 0, \tag{4}$$

where the notation $\hat{\omega}=\omega+i\gamma m^2$ is introduced. This equation gives the structure of normal modes within the barotropic shear. It describes a continuous spectrum of inertia-gravity waves that are freely propagating, subinertial waves that are trapped in the anticyclonic shear region, and, possibly, unstable modes if the shear is strong enough.[22]

B. Explicit solutions for a tanh shear layer

Equation (4) was much studied in quantum mechanics in the particle-in-a-potential-well context, e.g., Ref. 25, and we can profit from this knowledge. The inertial instability of a tanh shear profile has previously been discussed[11] using an asymptotic approach which included finite along-stream wavenumbers. The analysis described below yields a compact and explicit form of the dispersion relation in the case with no along-stream variations both with and without the hydrostatic approximation.

We choose the standard representation of the shear flow:

$$U(y) = \tanh(y). \tag{5}$$

Note that the velocity and the length scales being already fixed, no parameter enters this definition. The profiles of M and Θ will change with $\mathcal{R}$, as follows from Eq. (2) and Fig. 1. Injecting Eq. (5) into Eq. (4) yields

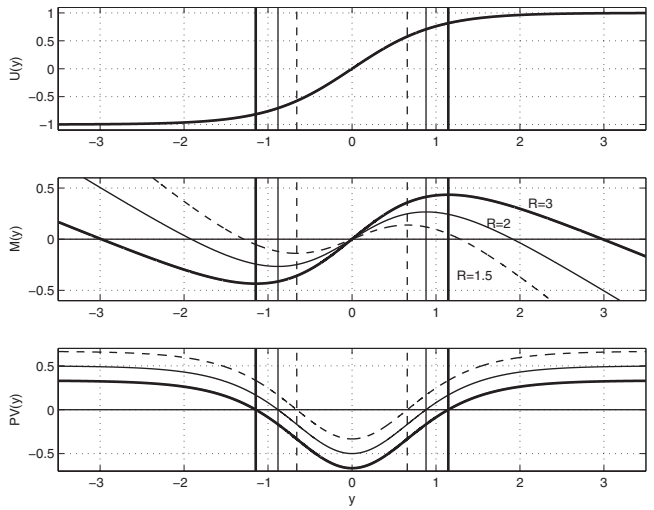

FIG. 1. Profile of velocity $U(y)$ (top), of geostrophic momentum $M(y)$ (middle), and of PV $Q(y)=\mathcal{R}^{-1}-U_y$ (bottom) for the basic state corresponding to three values of $\mathcal{R}$: 1.5 (dashed line), 2 (thin line), and 3 (thick line). Also indicated in both figures are the bounds of the unstable regions ($dU/dy > \mathcal{R}^{-1}$) for the three values of $\mathcal{R}$.

$$\hat{\psi}_{yy} + \frac{m^2}{1-\hat{\omega}^2\delta^2}\left[\hat{\omega}^2 - \left(1 - \frac{\mathcal{R}}{\cosh^2 y}\right)\right]\hat{\psi} = 0. \tag{6}$$

Following Ref. 25 we change variables as $\xi=\tanh(y)$ and transform this equation into

$$\frac{d}{d\xi}\left[(1-\xi^2)\frac{d}{d\xi}\right]\hat{\psi} + \left[s(s+1) - \frac{\epsilon^2}{1-\xi^2}\right]\hat{\psi} = 0, \tag{7a}$$

where

$$s(s+1) = \frac{m^2\mathcal{R}}{1-\hat{\omega}^2\delta^2}, \quad \epsilon^2 = \frac{m^2(1-\hat{\omega}^2)}{1-\hat{\omega}\delta^2}. \tag{7b}$$

Note that we have supposed that $\hat{\omega}^2 < 1$ to define ϵ.

Solutions that are finite for $\xi=1$ ($y \to +\infty$) are of the form

$$\hat{\psi} = (1-\xi^2)^{\epsilon/2} F\left[\epsilon - s, \epsilon + s + 1; \epsilon + 1; \tfrac{1}{2}(1-\xi)\right], \tag{8}$$

where F is the hypergeometric function (Ref. 26, Chap. 15). For ψ to remain bounded at $\xi=-1$ ($y \to -\infty$), we need to have

$$\epsilon - s = -n \quad \text{with} \quad n = 0,1,2,3,\ldots. \tag{9}$$

The parameter n corresponds to the number of nodes of $\psi(y)$: inside the "potential well," where $\hat{\omega}^2-(1-\mathcal{R}U_y)>0$, ψ oscillates and has n nodes. Outside the potential well the function $\psi(y)$ decays exponentially (e.g., Fig. 4 in Ref. 22).

The constraint (9), together with definitions (7b), yields the following dispersion relation:

$$\mathcal{G}(\hat{\omega}^2, m, n, \delta, \mathcal{R}) = 2m\sqrt{\frac{1-\hat{\omega}^2}{1-\delta^2\hat{\omega}^2}} + 2n + 1 - \sqrt{1 + \frac{4m^2\mathcal{R}}{1-\delta^2\hat{\omega}^2}} = 0. \tag{10}$$

For the configurations with $\delta \ll 1$ under consideration it turns out that this form is redundant. The hydrostatic limit ($\delta=0$) of the dispersion relation can be used instead:

Downloaded 14 Oct 2009 to 129.199.72.169. Redistribution subject to AIP license or copyright; see http://pof.aip.org/pof/copyright.jsp

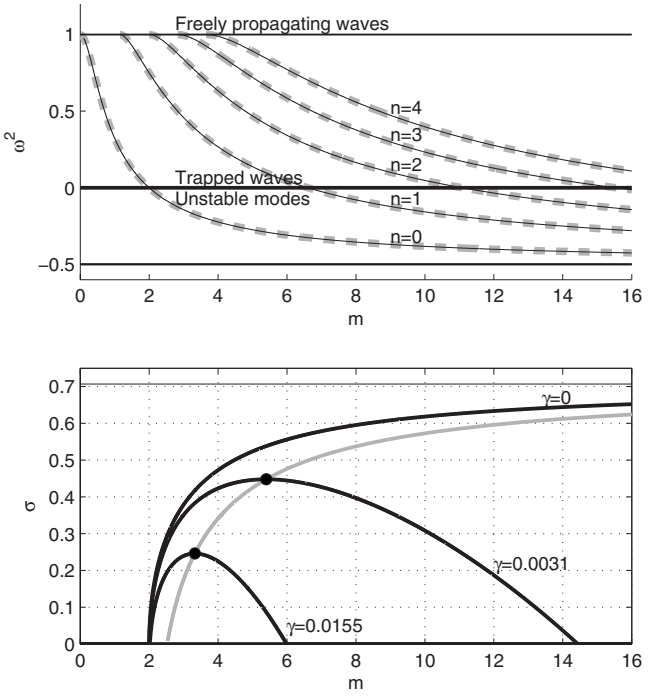

FIG. 2. Upper panel: Dispersion curves $\hat{\omega}^2(m)$ for $\mathcal{R}=1.5$ with $\delta=10^{-2}$ for $n=0-4$. Two sets of curves are shown: from the full expression (10) in thin black lines and from the hydrostatic expression (11) in thick, dashed, gray lines. Horizontal lines indicate the separation (thin line, $\hat{\omega}^2=1$) between the continuous spectrum of freely propagating waves and discrete spectrum of trapped waves, the separation (thick line, $\hat{\omega}^2=0$) between trapped waves and unstable modes, and the asymptote for the lowest value of $\hat{\omega}^2$ (thin line, $\hat{\omega}^2=1-\mathcal{R}=-0.5$). Lower panel: Growth rate σ as a function of the vertical wavenumber m for the fundamental mode $n=0$. The three curves correspond to $\gamma=0$, 3.10×10^{-3}, and 1.55×10^{-2}. Maximum growth rates are found on the thick gray curve as γ varies, tending for $\gamma\to0$ toward the asymptote shown as a thin black line.

$$\hat{\omega}^2 = 1 - \frac{1}{4m^2}(2n+1-\sqrt{1+4\mathcal{R}m^2})^2, \tag{11}$$

which is valid only for $\hat{\omega}^2<1$ [cf. Eq. (7b)], i.e., only for $m>\sqrt{n(n+1)/\mathcal{R}}$. The latter condition implies that there is always an interval of wavenumbers m close to zero that are stable. The width of this interval increases with n (Fig. 2).

The upper panel of Fig. 2 describes $\hat{\omega}^2$ obtained both by the hydrostatic [Eq. (11)] and nonhydrostatic [Eq. (10)] relations for a Rossby number $\mathcal{R}=1.5$ and $\delta=10^{-2}$. The curves are indistinguishable, which confirms that for the low values of δ, commonly found in the atmosphere, the hydrostatic limit is largely sufficient. We will use the form (11) in what follows.

C. Growth rates of the symmetric unstable modes

It is insightful to first examine the dispersion relation (11) in the inviscid case, i.e., when $\hat{\omega}=\omega$. For strongly anticyclonic flows ($\mathcal{R}>1$), $\hat{\omega}^2$ becomes negative for sufficiently large m (the corresponding mode then changes from a trapped subinertial wave[27] to an inertially unstable mode). Figure 2 shows that, as m increases, the $n=0$ mode is the first to become unstable, and it is followed by modes with increasing n. The growth rates increase monotonically with m and tend toward $\sigma_{\max}=\sqrt{\mathcal{R}-1}$ as $m\to\infty$ for all values of n, though more slowly as n increases.

The inclusion of diffusion in the vertical only modifies the definition of $\hat{\omega}=\omega+i\gamma m^2$. The growth rates of unstable inviscid modes diminish, and for large enough values of m these modes become decaying. Hence, as illustrated in the lower panel of Fig. 2, only a finite range of vertical wavenumbers m are unstable, and the maximum growth rate is attained at a finite value $m_{\max}$, in contrast to the inviscid case (well-defined scalings for the variation of $m_{\max}$ as $\gamma\to0$ can be obtained[28,29]). This fact will allow for well-resolved numerical simulations in what follows.

The linear theory provides not only the growth rates but also the structure of the modes. The streamfunction is $\psi(y,z,t)=\hat{\psi}(y)e^{i(mz-\omega t)}$, with $\hat{\psi}$ given by Eq. (8). Other variables are expressed in terms of $\hat{\psi}$ as follows:

$$\hat{u} = \frac{m}{\hat{\omega}}(1-\mathcal{R}U_y)\hat{\psi}, \quad \hat{v} = -im\hat{\psi}, \tag{12a}$$

$$\hat{w} = \frac{d\hat{\psi}}{dy}, \quad \hat{\chi} = -\frac{i}{\hat{\omega}}\frac{d\hat{\psi}}{dy}. \tag{12b}$$

The unstable modes are confined within the region with negative PV. Outside the region of anticyclonic vorticity, they decay exponentially. Within the unstable region, the most unstable mode ($n=0$) consists of a stack of overturning cells.[4]

III. LINEAR INSTABILITY IN NUMERICAL SIMULATIONS

The analytical solutions described above provide a benchmark for validation of the linear stage of the instability in the numerical simulations. The numerical setup of the simulations is described in Sec. III A and the comparison with the analytical solutions in Sec. III B.

A. Numerical setup and simulation parameters

The simulations were carried out with the Weather Research and Forecast model (WRF, version 2.2, Ref. 30), which allows both idealized simulations and real-case studies for atmospheric flows. Choosing a community model that has a wide range of capabilities and is widely used has several advantages: it makes it easier for other investigators to reproduce present results, and what is more important, it opens the possibility, in further studies using the same model, to increase the complexity and realism of simulations (three dimensions, incorporation of moist processes) and to move toward case studies which can be compared with observations (e.g., for air masses advected from one hemisphere to the other, as described in Refs. 5 and 6).

The model integrates the equations for a fully compressible, nonhydrostatic atmosphere in flux form with terrain-following hydrostatic pressure as the vertical coordinate.[30] The prognostic variables are the velocity components, the potential temperature, the geopotential, and the surface pressure, and they are discretized using a staggered Arakawa C

Downloaded 14 Oct 2009 to 129.199.72.169. Redistribution subject to AIP license or copyright; see http://pof.aip.org/pof/copyright.jsp

grid. The equations are integrated in time using a time-split third order Runge–Kutta scheme with a smaller time step for acoustic modes. The top of the model is a constant pressure surface.

One implication of using WRF is that the simulated flows will differ in several aspects from the flows for which analytical solutions were obtained: the model describes the evolution of a compressible atmosphere, whereas the Boussinesq approximation was used in Sec. II. The fluid is bounded below by a rigid, flat bottom with free-slip conditions, and the upper boundary condition corresponds to a free surface with constant pressure. Lateral walls with free-slip boundary conditions close the domain in the transverse direction. Finally, in order to provide dimensionful variables for the code, the horizontal length scale $L=25$ km for the width of the shear zone was chosen. The domain used for the simulations has dimensional width of 1000 km and a height of about 10 km (the last model level is an isobaric surface; its geometric height is not constant). The dimensional Coriolis parameter is $f=10^{-4}$ s^{-1}, so that one nondimensional time unit will correspond to $1/f=2.78$ h dimensionally.

Preliminary simulations showed that the top and bottom boundary conditions introduced undesired effects if the barotropic shear was taken to extend throughout the whole computational domain. Indeed, the unstable mode would not grow homogeneously in the vertical but would be strongly enhanced near the top boundary. This is presumably due to the free surface condition at the top boundary, which allows fast surface modes to exist and propagate with a strong signature near the top of the domain. In consequence, to avoid any influence of the top and bottom boundaries, the basic state was chosen to be a barotropic unstable shear in the center of the domain, decaying and becoming stable close to the top and bottom boundaries. By the thermal wind balance, this introduces horizontal gradients of temperature in the region where there is vertical shear. In order to limit the extent of these regions, the basic velocity was chosen to have a slow horizontal decrease far from the barotropic shear region:

$$U(y,z) = \tanh(y)(1/4) \times (\tanh[6(z/L_Z - 0.15)] - \tanh[6(z/L_Z - 0.85)]) \times (\tanh[12(y/L_H - 0.125)] - \tanh[12(y/L_H - 0.875)]), \quad (13)$$

where L_H and L_Z are the domain width and height. The resulting distribution of wind and potential temperature is displayed in Fig. 3. In the center of the domain, for $15<z<25$ and for $-10<y<10$, the flow is a barotropic shear with $U(y)=\tanh(y)$ as described in Sec. II, and the boundaries no longer affect the development of the instability, although they will play a role at late times due to the reflection of emitted gravity waves (see Sec. V B 3).

The initial fields for velocity and temperature were obtained numerically by solving iteratively for the pressure so that the geostrophic zonal wind corresponds to the one prescribed and that the stratification be such that $\delta=10^{-2}$ on average. Wind was deduced from geostrophic equilibrium and potential temperature was obtained from hydrostatic balance.

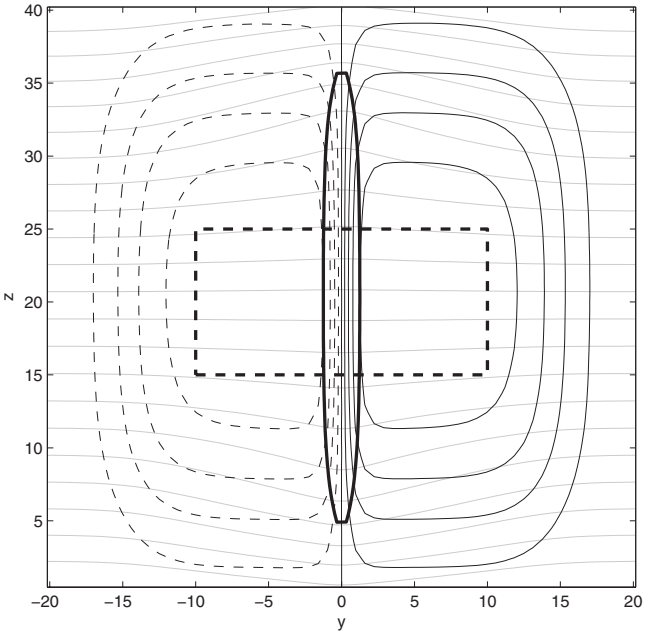

FIG. 3. Contours of the zonal velocity $U(y,z)$ of the basic state (black lines, dashed for negative values, contour integral of 0.2) and potential temperature (thin gray lines) for simulations with $\mathcal{R}=3$. Horizontal axis is y, nondimensionalized by $L=25$ km, and vertical axis is z, nondimensionalized by $fL/N=250$ m. Also shown is the zero contour of PV (thick black line) and the region in which the flow is well approximated as a barotropic shear (dashed line).

More than 50 simulations were carried out, varying the Rossby number $\mathcal{R}$, the diffusion γ, and resolution as described in Table I. Corresponding Reynolds numbers range from 20 to 1000 in the simulations where explicit diffusion was included. Simulations will be referenced below by the values of these numbers: for example, simulation $\mathcal{R}2$-$\gamma 1$-$r3$ corresponds to a Rossby number $\mathcal{R}=2$ and a diffusion parameter $\gamma=3.10\times10^{-3}$ simulated at resolution 128×128.

For each simulation, a breeding procedure was used to isolate the most unstable growing mode: a simulation is started with a small random perturbation in the temperature field. After 4.3 nondimensional time units (12 h dimensionally), the anomaly relative to the initial state is isolated, rescaled to a small amplitude, and added to the basic state to start a new simulation. This cycle is repeated five times. A

TABLE I. Summary of the various parameter values that were used in the two-dimensional simulations.

$\mathcal{R}$	Ekman number γ	Resolution
1.5	0: $\gamma=0$	1: 32×32
2.0	1: $\gamma=3.10\times10^{-3}$	2: 64×64
3.0	2: $\gamma=1.55\times10^{-2}$	3: 128×128
	3: $\gamma=7.75\times10^{-2}$	4: 256×256
		(5: 512×512)

Downloaded 14 Oct 2009 to 129.199.72.169. Redistribution subject to AIP license or copyright; see http://pof.aip.org/pof/copyright.jsp

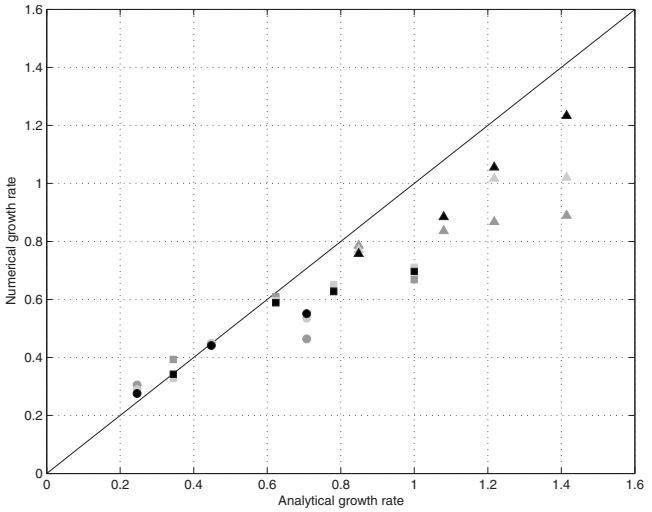

FIG. 4. Comparison of the analytical and numerically obtained growth rates. Circles correspond to runs with $\mathcal{R}=1.5$, squares for $\mathcal{R}=2$, and triangles for $\mathcal{R}=3$. Symbols are in black for resolution 4 runs, in gray for resolution 3, and in light gray for resolution 2. For a given set of symbols, the analytical growth rate increases as the Ekman number decreases from $\gamma=7.75\times10^{-2}$ to $\gamma=1.55\times10^{-2}$ to $\gamma=3.10\times10^{-3}$ and finally 0. For $\mathcal{R}=1.5$, flows with $\gamma=7.75\times10^{-2}$ were stable.

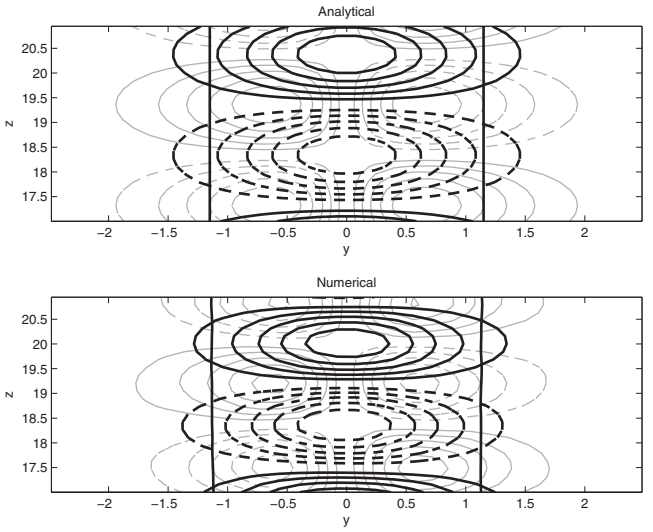

FIG. 5. Meridional (thick black line) and vertical (thin gray line) velocity isolines for the most unstable normal mode of a barotropic shear with $\mathcal{R}=3$ and $\gamma=7.76\times10^{-2}$. The analytical solution (top panel) compares very well with the numerically obtained normal mode (bottom panel). Contours correspond to the same values on both panels ($\pm1/6[1,2,3,4,5]$ of the maximum value of v and w, with negative contours dashed), and the bounds of the unstable region are shown (vertical lines).

simulation was then restarted in 52 nondimensional time units with this mode present in the initial condition with a weak amplitude.

B. Comparison with analytical predictions

The availability of analytical solutions for the linear stability problem provides a benchmark for the numerical simulations. The growth rates and the structure of the modes obtained numerically are found to agree well with those obtained analytically for configurations which were sufficiently diffusive (Fig. 4). If one takes into account the finite resolution while calculating the theoretical maximum growth rate, the agreement improves for the simulations with $\gamma=0$. Finally, the agreement is not as good for the strongly unstable case ($\mathcal{R}=3$), in part because the breeding procedure was less successful in isolating the unstable mode in a clean way (the breeding cycles were too long to ensure that only linear growth occurred) and in part because of insufficient resolution (theoretically, one would expect modes close to the grid scale).

The structure of the numerically obtained modes is also in agreement with that predicted theoretically. It is illustrated in Fig. 5 by the structure of the meridional velocity for simulation $\mathcal{R}3$-$\gamma3$-$r4$. Both the analytical and the numerically obtained normal modes are shown. The simulated normal mode has a slightly smaller vertical wavelength, but the two structures are otherwise essentially the same.

IV. NONLINEAR SATURATION

The linear normal mode solution describes an overturning motion (Fig. 5), and uninterrupted growth of these motions will lead to static instability in a finite time. For sufficiently diffusive flows, however, it is known that a purely diffusive equilibration may occur, as described for the case of a constant shear at the equator in Ref. 15. A simple scenario of nonlinear saturation of the instability can be identified in strongly diffusive simulations (Sec. IV A). Essential features of this scenario persist in weakly diffusive simulations as well, although small-scale motions become much more active (Sec. IV B). Sensitivity to the numerical setup is discussed in Sec. IV C.

A. Strongly diffusive simulations

For strongly diffusive flows, it is expected from previous studies that the instability will grow and then decay, leaving behind a modified mean flow.[15] For strongly unstable situations, the unstable mode is expected to deform and affect a region wider than the initially unstable region.[15,18] We focus below on two specific signatures of this strongly nonlinear case: nonlinearity manifests itself in the horizontal spreading of the unstable motions and in the temporary enhancement of the maximum anticyclonic vorticity.

Figure 6 depicts the evolution of the unstable mode in the strongly diffusive and strongly unstable simulation $\mathcal{R}3$-$\gamma3$-r4. The structure of the mode remains smooth and well resolved, and the mode spreads horizontally once it has reached finite amplitude. This can be understood as a consequence of the modification of the background stratification (weaker stratification ahead of the transverse flow, see Fig. 6, favors spreading). The resulting alternating northward and southward jets do not induce an overall mass flux but do induce a negative flux of geostrophic momentum.

During this process of horizontal spreading, a somewhat counterintuitive effect occurs ahead of the transverse jets. In such regions, the fluid undergoes considerable vertical stretching, as can be seen in the middle column of Fig. 6. For parcels which are initially unstable, absolute vorticity initially is negative, and the stretching therefore amplifies the

Downloaded 14 Oct 2009 to 129.199.72.169. Redistribution subject to AIP license or copyright; see http://pof.aip.org/pof/copyright.jsp

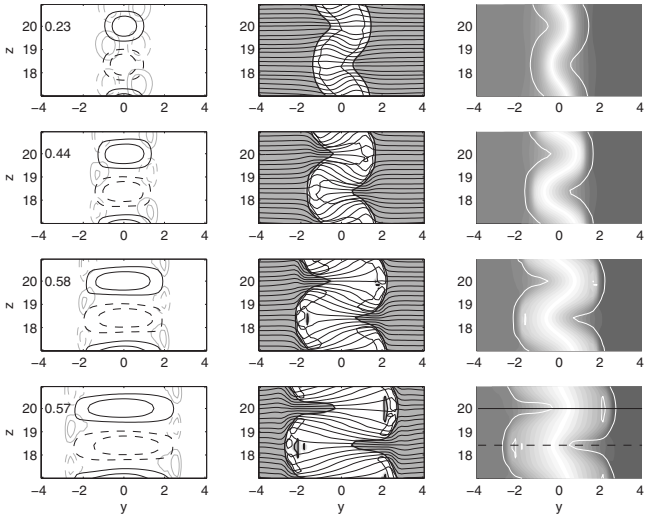

FIG. 6. Horizontal spreading of the unstable mode in simulation $\mathcal{R}3$-$\gamma 3$-$r4$ for nondimensional times $t=2.9$, 4.4, 5.8, and 7.2, from top to bottom. Left: meridional and vertical velocity, as in Fig. 5 but with less contours for clarity [contours are for 1/3 and 2/3 of max($\|v\|$), indicated in the top left]. Middle: isolines of potential temperature and of PV [gray shading for positive PV and contours for PV=0 (thick line) and PV=0.25 (thin line)]. Right: velocity (shading) and PV=0 contour (white line). Also shown in the lower-right panel are the heights corresponding to the profiles of relative vorticity presented in Fig. 7.

anticyclonic vorticity. This is illustrated in Fig. 7 by horizontal profiles of the relative vorticity taken at the center of a northward and a southward jet. Hence, although the instability is caused by the negative absolute vorticity, nonlinear evolution temporarily produces its significant intensification (more than doubling, see Fig. 7). This is reminiscent of the behavior described by Griffiths[15] for $f\bar{Q}$, where $\bar{Q}$ is the vertically averaged vorticity anomalies (paragraph 4.6 and Fig. 7 of Ref. 15). However, the equatorial problem has an asymmetry due to the β-effect such that enhanced negative vorticity anomalies are found only on the poleward side of the

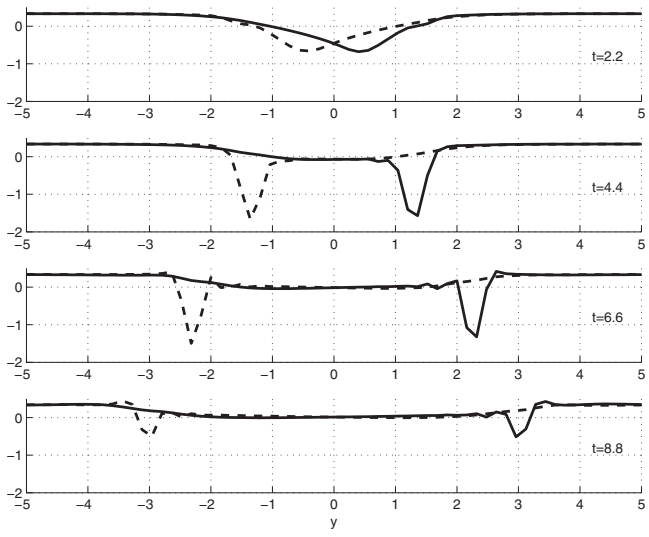

FIG. 7. Vertical component of the absolute vorticity at heights $z=20.0$ (plain line) and $z=18.4$ (dashed line) for simulation $\mathcal{R}3$-$\gamma 3$-$r4$ (as in Fig. 6, as a function of y) at four successive nondimensional times, $t=2.2$, 4.4, 6.6, and 8.8, from top to bottom.

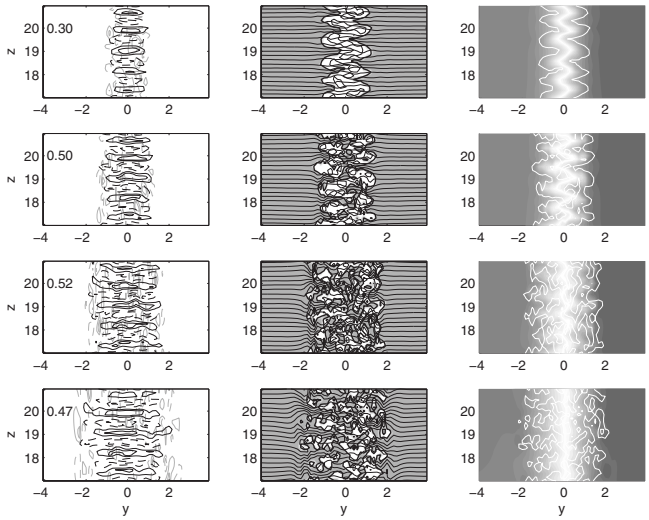

FIG. 8. Same as in Fig. 6 but for simulation $\mathcal{R}2$-$\gamma 0$-$r4$.

unstable region. In contrast, the vorticity anomalies described above appear on both sides of the initially unstable region, at different heights.

Finally, the saturation of the instability can be understood as follows: as the mode spreads out, the column of negative PV becomes severely distorted, in such a way that meanders offer strong vertical gradients for diffusion to act upon (middle and right columns of Fig. 6). The distribution of zonal velocity then returns to a barotropic configuration, with the anticyclonic shear spread out over a wider region (right column in Fig. 6) so that the flow is stabilized (the width of this region in the final state is discussed in Sec. V).

B. Weakly diffusive simulations

The strongly diffusive simulations reveal a clear and simple picture of the nonlinear development of the instability. For simulations with weaker diffusion, small-scale instabilities come into play and make the structures more complicated (Fig. 8). No special parametrization is used in the model to deal with KH instabilities, and it is numerical diffusion which takes care of them, in contrast to the simulations in Ref. 16.

Nevertheless, two of the main features outlined above persist and appear to be generic: the horizontal spreading and the increase in the minimum relative vorticity are found systematically in the simulations. The nonlinear spreading is found in all simulations regardless of diffusion and resolution and will be explained by the tendency of the fluid toward a neutrally stable end state in Sec. V. The evolution of the minimum of the relative vorticity is quantitatively comparable in all the high-resolution simulations of the strongly unstable shear ($\mathcal{R}=3$, middle panel of Fig. 9). However, at lower resolutions the localized enhancement of relative vorticity nearly disappears, emphasizing the importance of resolution for this effect. This sensitivity to resolution is not surprising for a quantity that is a spatial derivative. When the shear is weakly unstable ($\mathcal{R}=1.5$ or $\mathcal{R}=2$ with strong diffu-

Downloaded 14 Oct 2009 to 129.199.72.169. Redistribution subject to AIP license or copyright; see http://pof.aip.org/pof/copyright.jsp

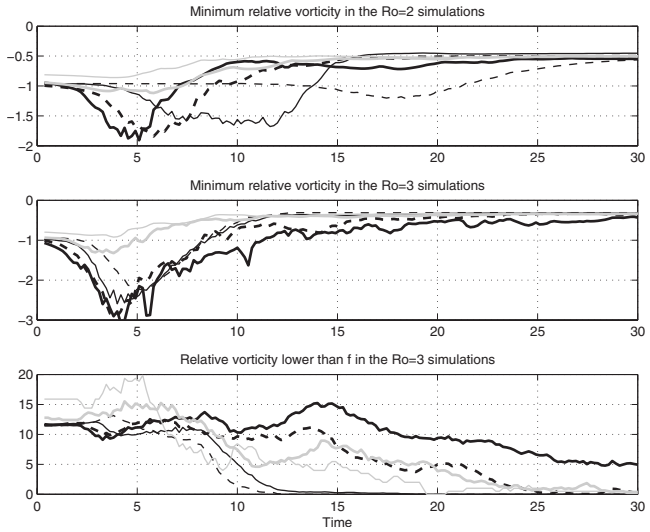

FIG. 9. Minimum of the relative vorticity $-\partial_y u$ in the domain $-10<y<10$ and $17<z<21$ for $\mathcal{R}=2$ (upper panel) and for $\mathcal{R}=3$ (middle panel) and percentage of points for which the absolute vorticity $\mathcal{R}^{-1}-\partial_y u$ is negative (lower panel) as a function of time. Results are shown for simulations at resolution 4 (black lines) for $\gamma 0$ (thick line), $\gamma 1$ (thick dashed line), $\gamma 2$ (thin line), and $\gamma 3$ (thin dashed line). Also shown are the results for $\gamma 0$ at resolutions 3 (gray thick line) and 2 (gray thin line).

sion) the enhancement of anticyclonic vorticity is reduced because the horizontal spreading becomes too slow relative to diffusion (upper panel of Fig. 9).

Yet, there are significant differences between weakly and strongly diffusive simulations. First, some regions of the flow become susceptible to small-scale KH instabilities (at small Richardson numbers), as well as static (convective) instability when $\mathcal{R}=3$, see Fig. 10. In consequence, the flow becomes more complex, and the evolution of the region with PV <0 differs. The initially unstable region is broken up into smaller and smaller pockets of negative PV (see Fig. 8), and

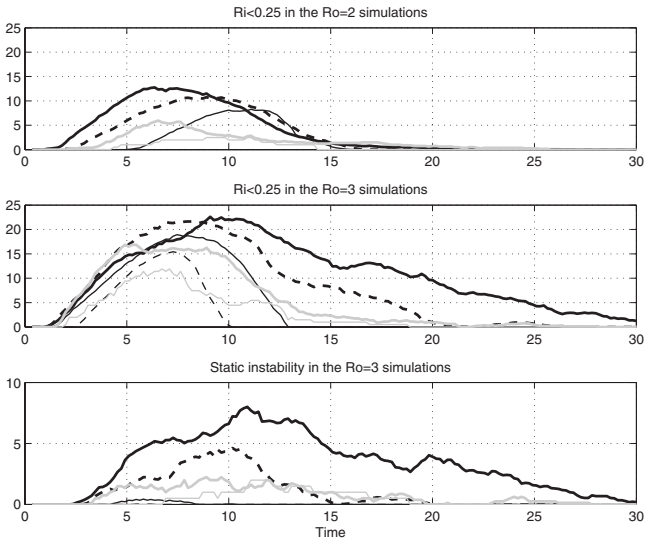

FIG. 10. Percentage of the volume of fluid in the domain $-10<y<10$ and $17<z<21$ for which the Richardson number is lower than 1/4 (upper panel, for simulations with $\mathcal{R}=2$ and middle panel, for simulations with $\mathcal{R}=3$) and for which there is static instability (lower panel, for $\mathcal{R}=3$). Lines are as in Fig. 9.

regions with negative anticyclonic vorticity persist for much longer time than in the diffusive simulations (lower panel of Fig. 9). Hence, in strong contrast to the more diffusive simulations, well-identifiable small-scale structures persist even once the barotropic component of the flow has reached a stable state, with remaining patches of negative PV and negative absolute vorticity, as described in Ref. 23 (Fig. 8 and the lower panel of Fig. 9). Long-lasting small-scale structures are further discussed in Sec. V.

A few remarks are in order regarding the behavior of the model when no explicit diffusion is included, i.e., when $\gamma=0$. First, simulations with $\gamma=0$ and $\gamma=3.10\times10^{-3}$ are quite comparable for the development and saturation of the instability, which gives us an indication regarding the level of numerical diffusion in the model. It is also found that the simulations are much more sensitive to $\mathcal{R}$ than to γ, and in consequence that the use of these two parameters separately has advantages relative to the use of the Reynolds number $\mathrm{Re}=\mathcal{R}/\gamma$. Second, we calculated the evolution of the total energy of the flow for simulations with $\gamma=0$, as conservation of energy is not expected for flows involving instabilities down to the grid scale. From theoretical arguments we can predict what portion of kinetic energy ΔE_K is expected to be removed from the barotropic component of the flow by the instability (see Sec. V). In simulations with $\gamma=0$, we found that the kinetic energy loss agreed very well with this prediction, and that the loss of total energy was comparable to or smaller than ΔE_K. For example, for $\gamma=0$ and $\mathcal{R}=3$ the total energy loss was equal to 80% of ΔE_K, i.e., that 20% of the kinetic energy loss had been converted to potential energy (see Sec. V B 1). Hence, although we do not control the numerical diffusion, simulations with $\gamma=0$ exhibit satisfactory energetics and are hence useful to provide insights regarding the instability and its signature in weakly diffusive flows (the disadvantage of simulations with $\gamma=3.10\times10^{-3}$ being that the vertical diffusion, although weak, affects the vertical stratification and damps the small-scale features that persist after the instability has saturated).

C. Sensitivity to other effects

To investigate the sensitivity of the simulations to other effects, numerical experiments were carried out with the hydrostatic approximation, with a third dimension and with higher resolution. For all simulations described above, the model was used in nonhydrostatic mode. The importance of nonhydrostatic effects was tested by switching on the hydrostatic option in WRF and revealed only a little difference as could be expected for the parameter regime considered ($\delta=10^{-2}$). The linear growth rates of the modes were barely changed. The end states were very similar: in strongly diffusive simulations the differences in velocities were typically smaller than 1%. In weakly diffusive simulations, final states were comparable, with small-scale fluctuations having similar amplitudes, length scales, and overall structure, though individual details did not match.

As a crude preliminary investigation of the potential modifications arising from three-dimensional (3D) effects, simulations were also carried out in a 3D setting, with 20

Downloaded 14 Oct 2009 to 129.199.72.169. Redistribution subject to AIP license or copyright; see http://pof.aip.org/pof/copyright.jsp

points in the x direction, at resolution $r3$. The initial state was perturbed with random noise in the potential temperature. It turns out that the resolution used is insufficient to observe any changes in the development of the instability. The rms of fluctuations in the x direction remains stationary during the simulation, and differences in the end states are minor and small scale (e.g., for u, less than 4% for $\gamma 0$) and decreases further as diffusion increases (less than 2% for $\gamma 1$, less than 0.4% for $\gamma 2$). These simulations indicate that if 3D effects modify the development of the instability as suggested in Ref. 16, higher resolution is necessary to capture them. In fact, in order to investigate these 3D effects and to describe the cascade of instabilities involved would require not only multiplying the size of our domains by the number of points in the third dimension, e.g., 20, but also increasing the resolution so that KH instabilities, which are nonhydrostatic, can be described. A dramatic increase in resolution (factor of $1/\delta$) and hence of computing resources or a different strategy (smaller values of δ) will be necessary to investigate rigorously these 3D effects.

Finally, two simulations ($\mathcal{R}=3$, $\gamma 0$ and $\gamma 1$) were also carried out at a higher resolution ($r5$) to investigate further the sensitivity to resolution. The results were similar to the corresponding simulations at resolution 4, yet with some additional small-scale details (see Sec. V B).

V. THE FINAL STATE

The previous sections have focused on the development of inertial instability in its linear (Sec. III) and nonlinear phases (Sec. IV). The next question is to examine the end state toward which the fluid is evolving.

Two preliminary remarks need to be made at this stage: first, the flows considered are constrained to be two dimensional. Geostrophically balanced flows are then stationary solutions of the full equations and, if stable, are the most natural candidates for the final adjusted state. Stability of such states is guaranteed if PV is everywhere positive. Second, the problem is reminiscent of the geostrophic adjustment problem for a two-dimensional jet or front.[31–34] The final adjusted state for an arbitrary initial condition with everywhere positive PV can be determined unambiguously, being entirely defined by the conservation of M and θ.[22] The flows with strong (but stable) anticyclonic shears may contain subinertial waves[22,27] trapped in the anticyclonic region, and hence modifying the standard geostrophic adjustment scenario.[35]

The present problem may be viewed in this context as an adjustment toward an unstable state. Naturally, this latter cannot be achieved because the instability drives the system to another, stable, adjusted state which cannot be predicted uniquely from the conservation laws, as nonlinear saturation of the instability requires dissipation (cf. Ref. 36 for a similar situation but with another type of instability).

Predictions for the barotropic component of the final state were given in Ref. 20 (in the case of rectilinear flows) and Ref. 19 (in the case of axisymmetric flow). They are based on conservation of total linear or angular momentum, respectively. In particular, in Ref. 20 the instability of a mixing layer similar to the flows we consider is described but with $U(y) \propto \mathrm{erf}(y)$.

Hence two questions arise considering the development of inertial instability as an adjustment problem:

(1) How close does the barotropic component of the flow come to the adjusted state predicted in Ref. 20 at the end of our simulations?
(2) What are, if any, the baroclinic fluctuations around this adjusted state?

Obviously, the sensitivity to the model parameters (resolution, diffusivity) should be investigated while answering both questions.

A. Predictions for the final state

We first recall the prediction of the final state, as given by Kloosterziel *et al.*[19] It is natural to assume that the instability suppresses the regions of negative PV. For a barotropic jet, the instability may be inferred from the plots of the vertically averaged geostrophic momentum $\bar{M}(y)=(z_2-z_1)^{-1}\int_{z_1}^{z_2} M dy$: unstable regions are those where M increases with y, and marginally stable regions are those where M is constant in y.

As explained in Ref. 19, a tentative final state can be obtained from a Maxwell rule applied to the plots of M (Fig. 1). The initial state, $\bar{M}_i(y)=M_i(y)=U(y)-\mathcal{R}^{-1}y$, is unstable where $\partial \bar{M}_i/\partial y>0$. Let $\bar{M}_f(y)$ describe the vertically averaged final state. It is natural to assume marginal stability $\partial \bar{M}_f/\partial y \le 0$ everywhere and $\bar{M}_f(y)=\bar{M}_i(y)$ far from the initially unstable zone. Graphically, this means that the region of increasing $\bar{M}_i$ in Fig. 1 is replaced by constant $\bar{M}_f$ in a larger region $y_1<y<y_2$, such that $\bar{M}_i(y_1)=\bar{M}_f(y_1)$ and $\bar{M}_i(y_2)=\bar{M}_f(y_2)$. In general one more constraint is needed to determine the region of uniform $\bar{M}_f$. This additional constraint is the conservation of momentum: $\int_{y_1}^{y_2}\bar{M}_f(y)dy = \int_{y_1}^{y_2}\bar{M}_i(y)dy$.

In the antisymmetric configurations considered here, the final state is given by

$$\bar{M}_f(y)=0 \quad \text{for} \quad -Y<y<Y,$$
$$\bar{M}_f(y)=M_i(y) \quad \text{for} \quad |y|>Y \quad \text{with} \quad \frac{Y}{\mathcal{R}}=\tanh Y, \tag{14}$$

where Y is the positive, nonzero root of $M_i(Y)=0$ (see Fig. 1).

The barotropic component of the simulated flows at late times was compared with this simple prediction. The agreement is remarkable, as shown in plots of zonal velocity (Fig. 11), and there is surprisingly small sensitivity to resolution and diffusion. Some sensitivity does appear on the plots of the geostrophic momentum in Fig. 12, showing a better agreement as resolution is increased. In particular, in weakly diffusive simulations and at high enough resolution, the flow is modified beyond $[-Y,Y]$, which is consistent with "over-

Downloaded 14 Oct 2009 to 129.199.72.169. Redistribution subject to AIP license or copyright; see http://pof.aip.org/pof/copyright.jsp

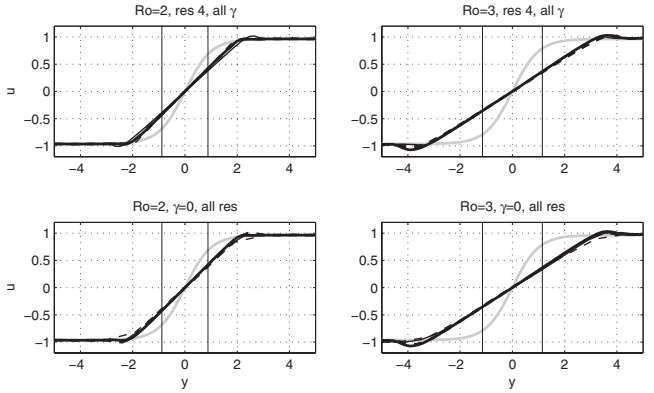

FIG. 11. Vertically averaged zonal velocity, between $z=17$ and $z=23$, in the final states [averaged for one inertial period (2π) around $t=31$]. The initial velocity $U(y)$ (thick gray line) and the bounds of the unstable region (thin vertical lines) are shown for reference. Left column shows results from simulations with $\mathcal{R}=2$ and right column for simulations with $\mathcal{R}=3$. Upper panels show four curves corresponding to the different values of γ used, while the lower panels show four curves corresponding to resolutions 1–4. Lines correspond to increasing γ (or decreasing resolution) in the following order: thick, thick dashed, thin, and thin dashed.

shoots" occurring during the nonlinear spreading of the unstable motions.[20] Yet, this sensitivity is less important than in Ref. 20 possibly because the simulations in Ref. 20 had higher Reynolds numbers and included horizontal diffusion. In order to illustrate the adjustment to the final state, we show in Fig. 13 the profiles of $\bar{M}(y)$ at different times for simulation $\mathcal{R}2$-$\gamma 0$-$r4$. The adjustment is very rapid (of the order of an inertial period) and, interestingly, after the initial adjustment stage $\bar{M}(y)$ hardly fluctuates at all.

The availability of a simple and efficient prediction of the final state allows to calculate analytically the excess kinetic energy to be removed from the barotropic component of the flow by the developing instability. This possibility was discussed for vortices[19] and for barotropic shear profiles.[20] There are good reasons to believe that the final state constructed with the method above always has less energy than the initial state.[20] In the present case, the energy loss can be obtained from the profiles of initial and final velocities, $u_i = U$ [Eq. (5)], and $\bar{u}_f$ deduced from Eq. (14):

$$\Delta E_K = \int_{-\infty}^{\infty} (\bar{u}_i^2 - \bar{u}_f^2) dy = \int_{-Y}^{Y} \left(\tanh^2(y) - \frac{y^2}{\mathcal{R}^2} \right) dy = 2Y \left(1 - \frac{1}{\mathcal{R}} - \frac{Y^2}{3\mathcal{R}^2} \right), \tag{15}$$

where we have used the facts that $\int_{-Y}^{Y} \tanh^2(y) dy = 2(Y - \tanh Y)$ and $\tanh Y = Y\mathcal{R}^{-1}$. For large $\mathcal{R}$, $Y \sim \mathcal{R}$ and the latter expression is readily approximated as

$$\Delta E_K \sim \tfrac{4}{3}\mathcal{R} - 2. \tag{16}$$

Kloosterziel *et al.*[20] compared the energy loss according to their prediction and in numerical simulations for four barotropic shear profiles and found reasonable agreement. As discussed below, our simulations confirm the relevance of this prediction for the energy loss by the mean barotropic flow for moderate and high Reynolds numbers.

Thus, our simulations suggest that the barotropic, geostrophically balanced part of the final state is well predicted from simple arguments, and that the adjustment toward this state is achieved, basically, regardless of resolution or dissipation. Two final remarks are in order. First, this conclusion applies to flows that are indeed unstable (strong enough diffusion may inhibit the instability altogether), and one may expect a somewhat different scenario for the flows just over the stability threshold:[15] diffusion can inhibit instability for regions with weakly negative PV. Hence, in such a case the equilibration of the instability does not necessarily lead the fluid to a state with zero PV but rather a state with a weak, negative PV. Second, in the present case (barotropic state, away from boundaries), the equilibration of the flow necessarily involved lateral mixing with fluid having positive PV. In cases where the unstable region has a small vertical extent or when the domain boundaries are close to the unstable region, equilibration may also involve entrainment of fluid with positive PV from above and below[17] or fluxes from the boundaries.[23]

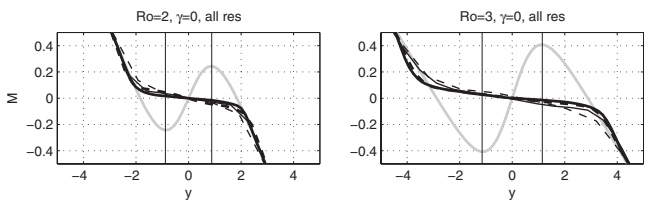

FIG. 12. Same as the lower panels in Fig. 11 but for the vertically averaged geostrophic momentum.

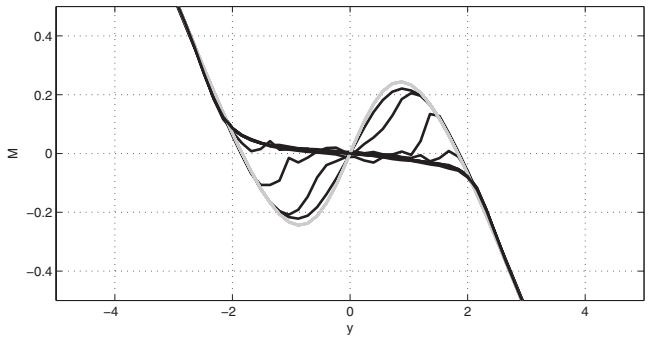

FIG. 13. Vertically averaged geostrophic momentum between $z=17$ and $z=23$ for the simulation with $\mathcal{R}2$-$\gamma 0$-$r4$, as in Fig. 14, left panel, with the addition of intermediate states (thin lines for $t=0.25, 0.5, 0.75, 1, 2, 3, \ldots, 8$).

B. Small-scale fluctuations in the final state

Whereas the barotropic component of the flow has a simple and robust behavior, the baroclinic component of the end state will be much more sensitive to resolution and dissipation. Yet, for large enough Rossby numbers this component is essential. It has hitherto attracted little attention and will be analyzed below.

The baroclinic fluctuations are small scale and fall into three categories: permanent layering in stratification, resulting from the mixing during the nonlinear stage of the instability (Sec. V B 1), subinertial oscillations remaining in the

Downloaded 14 Oct 2009 to 129.199.72.169. Redistribution subject to AIP license or copyright; see http://pof.aip.org/pof/copyright.jsp

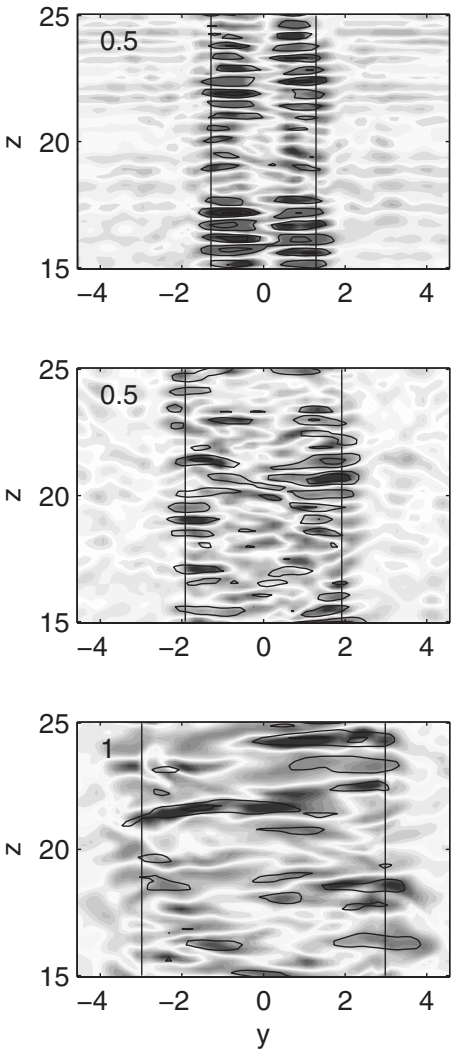

FIG. 14. Instantaneous intensity of the stratification $\partial_z \chi$ at late times ($t=39$) of simulations with resolution 4, $\gamma=0$, and $\mathcal{R}=1.5$ (top), $\mathcal{R}=2$ (middle), and $\mathcal{R}=3$ (bottom). Also shown are several isolines of the same field, averaged over 8.6 time units. Vertical lines indicate the bounds $[-Y$ and Y, cf. Eq. (15)] of the modified region in the predicted adjusted state, and maximum values of $|\partial_z \chi|$ are indicated in the upper left of each panel.

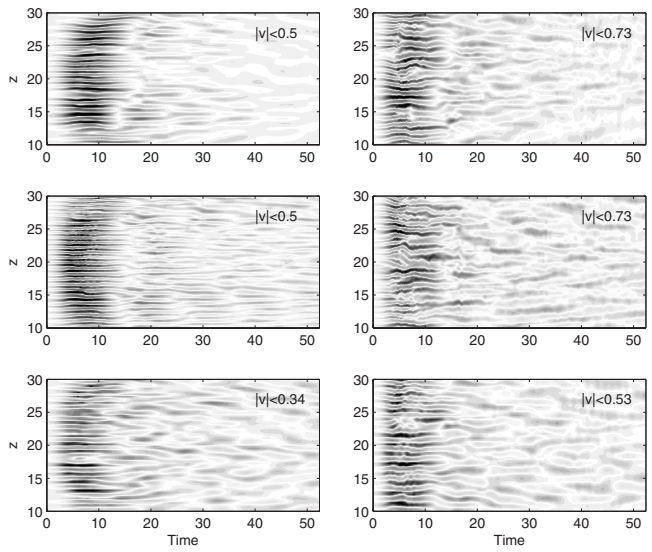

FIG. 15. Hovmöller diagrams of the meridional velocity at $y=0$. Left column: $\mathcal{R}=2$; right column: $\mathcal{R}=3$. First row: $\gamma=3.1\times10^{-3}$, resolution 4. Second row: $\gamma=0$, resolution 4. Third row: $\gamma=0$, resolution 3.

anticyclonic region (Sec. V B 2), and gravity waves freely propagating away from the unstable region (Sec. V B 3).

1. Modifications of the stratification: Layering

In the simulations with weak diffusion, stabilization of the flow involves small-scale mixing. Necessarily, in regions where the fluid is mixed, its stratification weakens. In adjacent regions, stronger stratification will be found, and as a result a "staircase" vertical profile of potential temperature may be expected. To check this we are looking below for persistent features in stratification $\partial_z \chi$.

Figure 14 shows vertical cross sections of stratification $\partial_z \chi$ at a late time of weakly diffusive simulations ($\gamma=0$). Persistent layers of alternating stronger and weaker stratification are clearly found in the adjusted region (between $-Y$ and Y). In addition, a reflectional asymmetry with respect to the central axis $y=0$ of the shear region clearly appears in the case of the simulation with $\mathcal{R}=1.5$, reminiscent of the antisymmetry of the stratification anomalies in the normal mode (Fig. 6).

As the Rossby number increases, the layering becomes less regular, but homogenization of layers becomes more intense, leading to distinct staircase patterns. Also, one can note that at large Rossby numbers the flow becomes modified outside the theoretically predicted range $[-Y, Y]$, as was already mentioned above. Similar indications of layering can also be found in the simulations of inertial instability at the equator (Fig. 7 of Ref. 16), which included a parametrization for KH instability.

Small-scale structures can also be found in the final PV field of the weakly diffusive simulations. Although PV and stratification anomalies are evidently related, the PV field is more irregular and does not exhibit the same layered structures. This can be explained by considering, for example, a region of strong stratification, with only vertical vorticity: depending on the sign of the absolute vorticity, this can yield either a positive or a negative PV anomaly.

2. Subinertial oscillations

A notable feature of the final state is that it retains a wide region (of nondimensional width $\sim 2\mathcal{R}$ for large enough $\mathcal{R}$) of strong anticyclonic vorticity. Trapping of subinertial waves is possible in such regions. They introduce significant local fluctuations as displayed by Hovmöller plots in Figs. 15 and 16 and are at the origin of a significant portion of the signal. The fact that those are indeed subinertial trapped waves is confirmed using Fourier transform in time of the meridional velocity at $y=0$ (Fig. 17), showing fluctuations dominating at frequencies around a third of the inertial frequency. This is consistent with the oscillations seen in Fig. 15, with typical nondimensional periods of about 20, i.e., close to $3\times 2\pi$.

Downloaded 14 Oct 2009 to 129.199.72.169. Redistribution subject to AIP license or copyright; see http://pof.aip.org/pof/copyright.jsp

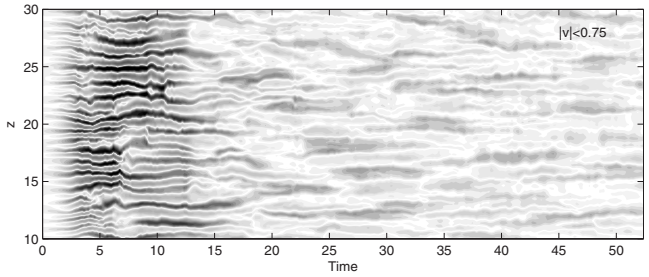

FIG. 16. Hovmöller diagram of meridional velocity for a simulation with $\gamma=0$ and $\mathcal{R}=3$, as in the right, middle panel of Fig. 11 but for resolution 5.

The importance of subinertial waves can be quantified relative to the prediction of ΔE_K [Eq. (15)]. Figure 18 shows the time evolution of the kinetic energy of the flow. First, the curves confirm that the energy loss in the simulations is fully consistent with the theoretical prediction: for all but strongly diffusive simulations, where energy is continuously dissipated, the ratio of the simulated energy loss to the theoretically predicted $|\Delta E_K|$ tends to -1. Second, they show fluctuations around the final value, indicative of the presence of subinertial oscillations for which kinetic energy is periodically converted to potential energy and vice versa. To quantify more precisely the energy that remains trapped in subinertial oscillations, Fig. 19 shows the time evolution of the baroclinic part of kinetic energy. In the weakly diffusive simulations ($\gamma0$ and $\gamma1$) for strongly unstable flow ($\mathcal{R}=3$) the baroclinic part of kinetic energy (mainly due to the subinertial oscillations) represents about 5%–10% of the kinetic energy loss two inertial periods after the saturation of the instability. This portion then slowly decays as the waves leak energy to freely propagating waves and are dissipated.

The trapped waves are sensitive to the Rossby number, to resolution, and to diffusion (Figs. 15 and 19). The sensitivity to diffusion is most important. Indeed, as the Rossby number increases, both the excess energy and the width of

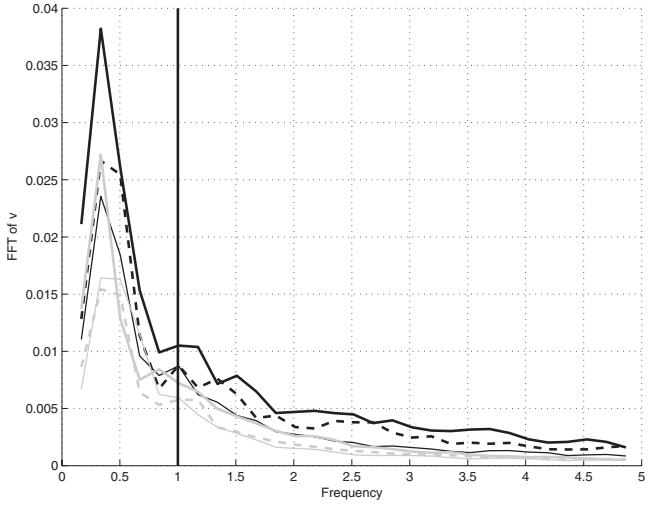

FIG. 17. Fourier transform in time of the meridional velocity at $y=0$, Fig. 15, for $10<z<30$ and for $t>15$. Results are shown for simulations with $\mathcal{R}=3$ (black lines) and $\mathcal{R}=2$ (gray lines), for resolution 4 and $\gamma0$ (thick lines), for lower resolution ($\gamma0$-$r3$ thin lines), and for moderate diffusion ($\gamma1$-$r4$ thick dashed lines).

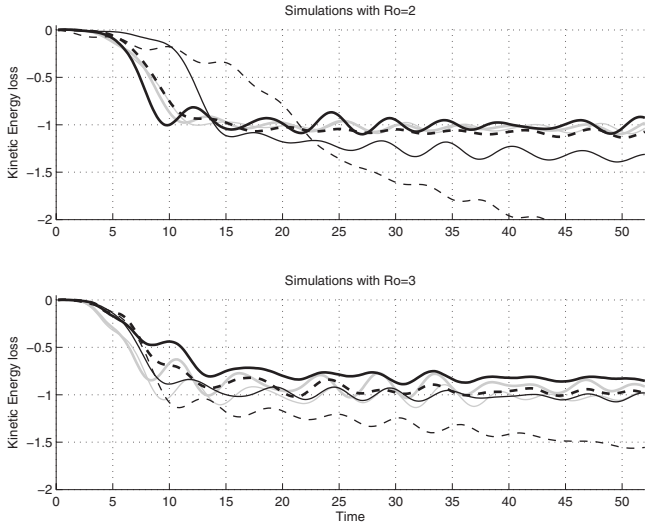

FIG. 18. Time evolution of kinetic energy anomaly relative to the initial state in the region $15<z<25$, scaled using the prediction for the final adjusted state [Eq. (15)]. Simulations shown correspond to resolution 4 (black lines), to $\mathcal{R}=2$ (upper panel) and $\mathcal{R}=3$ (lower panel), and to $\gamma0$ (thick lines), $\gamma1$ (thick dashed lines), $\gamma2$ (thin lines), and $\gamma3$ (thin dashed lines). Also shown are simulations at resolution 3 (gray lines) for $\gamma0$ (thick lines) and $\gamma1$ (thin lines).

the anticyclonic region in the final state increase. For large enough Rossby numbers the excess energy by unit length of the anticyclonic region tends to a constant. The effect of the vertical diffusion is to damp the waves, and they unavoidably decay in time. Resolution primarily restricts the vertical scale of these waves (compare the second and the last lines in Fig. 15), yet higher resolution does not lead to appearance of finer and finer waves (Fig. 16). Subinertial waves are virtually nonexistent in the strongly diffusive simulations (not shown). This is due in part to the dissipation of any oscillation but also to the slower development of the instability. As predicted by the linear theory (see Fig. 2), the growth rates are much smaller and hence the time scales are much larger, leading to a negligible excitation of inertia-gravity waves, trapped or not.

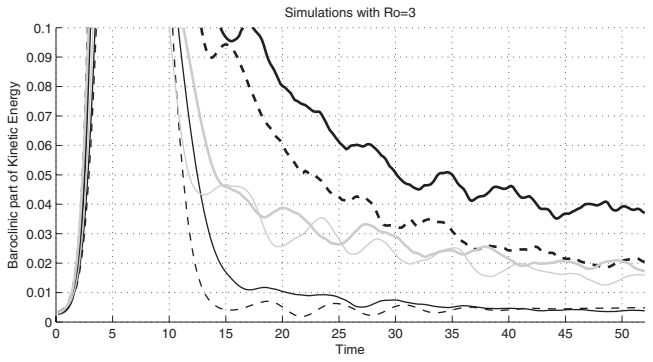

FIG. 19. Time evolution of the baroclinic part of the kinetic energy in the region $15<z<25$, scaled by the predicted kinetic energy loss relative to the initial state, for simulations with $\mathcal{R}=3$. Line coding is the same as in Fig. 18.

Downloaded 14 Oct 2009 to 129.199.72.169. Redistribution subject to AIP license or copyright; see http://pof.aip.org/pof/copyright.jsp

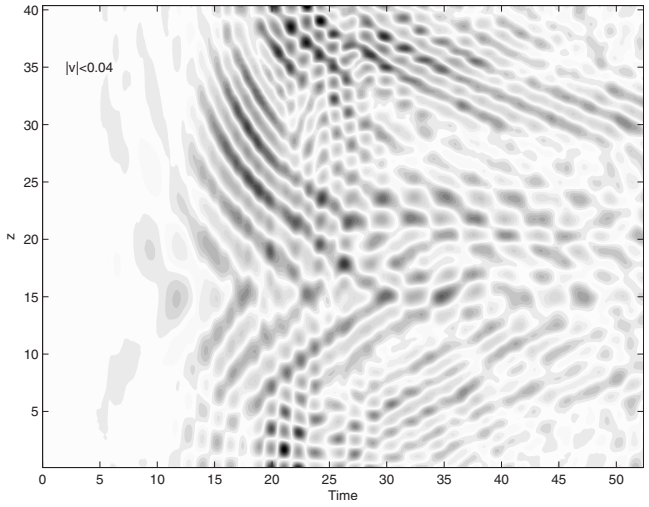

FIG. 20. Hovmöller diagram of the meridional velocity for $\mathcal{R}2$-$\gamma 1$-$r4$, $y=7.5$. Note that the vertical axis spans the whole domain, contrary to Fig. 15. Patterns of outward propagating waves are clearly seen between times 10 and 20. Beyond that time, reflections from the boundaries lead to interferences and more complex patterns.

3. Generation of free gravity waves

As mentioned above, the initial conditions are in geostrophic equilibrium. Hence, gravity waves produced during the evolution of the flow are not the result of a geostrophic adjustment of the initial condition but necessarily a product of the inertial instability. The possibility of gravity wave radiation by inertial instability was briefly discussed for axisymmetric vortices in Ref. 19, for which the radiation was found to be very small (at most 1/100 of the energy loss).

To illustrate the generation of these waves, Fig. 20 shows a Hovmöller plot similar to those in Fig. 11 but for a position far outside the unstable region. Two clear wavepackets are seen propagating away from the center of the domain (downward phase propagation for the top wave packet indicates upward propagation of energy and vice versa for the lower wave packet) several time units after the instability has saturated. The Fourier transform of these motions (Fig. 21) confirms that, in contrast to the motions described in Sec. V B 2, they are freely propagating low-frequency inertia-gravity waves. Their amplitudes are found to be weaker than those of the subinertial trapped modes roughly by a factor of 4.

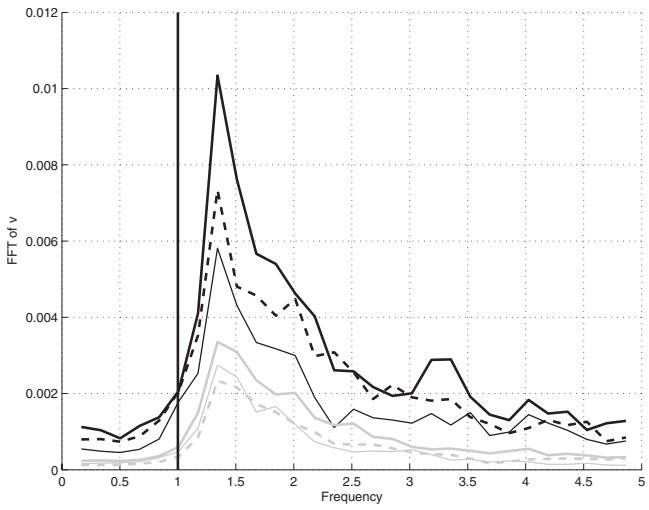

FIG. 21. Same as in Fig. 17 but for $y=7.5$.

There are several possible generation mechanisms of freely propagating gravity waves: the nonlinear evolution of the instability on time scales comparable to or faster than the inertial time scale is the major culprit for the generation of waves up to the saturation of the instability. After that, nonlinear interactions between subinertial trapped waves provide a weak but persistent source of low-frequency inertia-gravity waves.

This secondary production is again very sensitive to resolution and dissipation, making its quantification a difficult issue. Moreover, in the present setting the emitted waves are reflected from the boundaries and come back into the anticyclonic region. A more quantitative study of the excited waves is beyond the scope of the present paper and would require a different experimental setup, e.g., with a larger domain and sponge layers near the top, bottom, and lateral boundaries. Our emphasis here is merely to highlight the secondary generation in course of evolution of inertial instability as a source of gravity waves.

VI. SUMMARY AND DISCUSSION

The inertial instability of a barotropic shear in a continuously stratified and rotating fluid was investigated analytically and numerically, with a focus on two fundamental issues: the nonlinear stage of the instability and the end state of the flow evolution. A simple basic configuration was chosen: a flow on the f-plane, symmetric in x, thus excluding competition with barotropic instability (e.g., Ref. 10), with Prandtl number of 1, and the unstable shear chosen to be barotropic (purely *inertial* instability[2]).

The linear stability problem was solved analytically for the case of a barotropic shear $U(y)=\tanh y$ and explicit expressions were obtained for the dispersion relation and mode structure (Sec. II). As in the previous studies (e.g., Refs. 4 and 28), the largest growth rate is achieved in the inviscid limit, $\sigma_{\max}=\sqrt{\mathcal{R}-1}$, with $\mathcal{R}=U/fL$ the Rossby number, and is approached as the vertical wavenumber $m\to\infty$. The most unstable growing mode consists of overturning cells stacked in the column of negative PV.

The evolution of the instability was simulated numerically with the WRF model.[30] This choice allows for further investigation of the instability in more realistic flows with the same model. A breeding procedure was used to isolate the most unstable growing mode, which then served for the initialization of the simulations. The simulations ranged from strongly diffusive (Ekman number of 0.08), which were well resolved, to weakly diffusive (only numerical diffusion), which display the instabilities developing close to the grid scale. Yet the latter are more relevant to the atmosphere and ocean. A good agreement was found between the simulations and the analytical results at the linear instability stage (see Figs. 3 and 5), thus validating the numerical model.

Downloaded 14 Oct 2009 to 129.199.72.169. Redistribution subject to AIP license or copyright; see http://pof.aip.org/pof/copyright.jsp

Regarding the nonlinear development of the instability, the simulations revealed two generic features: horizontal spreading of the unstable mode beyond the region of initially negative PV and local intensification of the anticyclonic vorticity. Both can be easily understood in strongly diffusive simulations (Fig. 6): after an initial stage of self-similar growth, the unstable mode spreads laterally. Hence the initially barotropic band of negative PV is distorted by alternating transverse jets of increasing width. Sharp meanders form and are quickly diffused, yielding a new barotropic state. In the course of this saturation process, the horizontal spreading of the unstable motions leads to localized substantial intensification of the anticyclonic vorticity (Fig. 7). This effect is unexpected as it is precisely a strong anticyclonic vorticity which is at the origin of inertial instability. Note, however, that this increase in negative vorticity is compensated for by the decrease in stratification, leaving PV unaffected, which emphasizes that PV is indeed the appropriate quantity to analyze stability of stratified, rotating flows.

These generic features persist in the weakly diffusive simulations, although arising small-scale motions and instabilities significantly increase the complexity of the flow.

First, nonlinearity still leads to the horizontal spreading of the unstable mode (Fig. 8). In fact, the horizontal spreading occurs essentially regardless of resolution and diffusion, because the fluid tends to evolve toward a neutrally stable end state. This implies mixing of geostrophic momentum over a wider region than the initially unstable one, similar to the mixing of angular momentum by horizontally propagating dipole structures observed in simulations of inertially unstable barotropic vortices.[19] It is also, more remotely, reminiscent of the distortion experienced by a columnar vortex pair in the zigzag instability.[37] The horizontal spreading of transverse jets seen in the present simulations, however, always has a finite extent.

Second, the enhancement of anticyclonic vorticity in localized regions of the flow is again present, the minima of relative vorticity following comparable evolution regardless of diffusion (Fig. 9). Yet, this effect was observed to be very sensitive to resolution.

The weakly diffusive evolution of the instability contrasts with the strongly diffusive one in what concerns the small-scale instabilities (shear and convective ones) which provide necessary mixing of geostrophic momentum. In contrast to Ref. 16 no specific parametrization was set up to deal with KH instabilities. As a consequence of these small-scale instabilities, the region of negative PV is fragmented into smaller-scale patches[23] rather than smoothly diffused.

Regarding the end state of the flow evolution, we confirmed the prediction for the barotropic component based on conservation of momentum[20] and advanced by analyzing the baroclinic ones.

A prediction for a tentative final barotropic state[20] can be constructed graphically from the plots of geostrophic momentum M (Figs. 1 and 12): the initially unstable region (with $\partial M/\partial y > 0$) is replaced by a wider region of marginal stability ($\partial M/\partial y = 0$), the bounds of this region being defined following a Maxwell rule for the momentum. This prediction shows the necessity of the nonlinear spreading of the normal mode in order to mix geostrophic momentum over a region wider than the originally unstable one. In our simulations of unstable flows, the prediction was always fulfilled with little sensitivity to resolution and diffusion (Fig. 11). We thus confirm in a totally different model the findings in Ref. 20. Furthermore, as discussed previously for barotropic vortices[19] and for planar flows,[20] this construction provides an estimate of the energy lost by the flow due to the instability. Our simulations confirm the relevance of this analytic estimate of the excess kinetic energy to be removed by the instability.

The final state also contains baroclinic structures which are substantial for the weakly diffusive simulations and have not hitherto been analyzed in detail. For flows with weak diffusivity, apart from the straightforward dissipation the excess kinetic energy is transferred to three types of baroclinic perturbations:

(1) Permanent layers of stronger or weaker stratification. For strongly unstable flows ($\mathcal{R} \geq 3$), this leads to a characteristic staircase signature in vertical profiles of potential temperature.
(2) Trapped, subinertial gravity waves ($\omega < 1$, Ref. 27) in the marginally stable region ($-\partial \bar{u}/\partial y = -1$). These waves can slowly propagate vertically in the anticyclonic region but cannot escape from it.
(3) Freely propagating inertia-gravity waves, which are excited by the development of the instability and propagate away from the unstable region.

Our results show that inertial instability is a source of inertia-gravity waves,[38] which had only been mentioned once previously[19] to our knowledge. They also allow for interpretation of layered structures observed in velocity profiles of air advected from one hemisphere to the other.[5,6] Marginal stability, layering, and subinertial waves give a distinctive signature of a region that has undergone inertial instability. As all of the small-scale features detected in our simulations are sensitive to diffusion, quantification of their relative importance is still uncertain. Nevertheless, weakly diffusive simulations suggest that, right after the saturation of the instability, the excited inertia-gravity waves (trapped and free) could represent from 5% to 10% of the excess energy, the rest being removed by dissipation.

In the present study we considered only highly idealized flow configurations. The work with more realistic flows is in progress, with an emphasis on nonhydrostatic effects with weaker N/f (relevant for laboratory experiments), fully 3D simulations (cf. Ref. 16) and the role of a finite vertical extent of the unstable region (cf. Refs. 6, 17, and 39).

ACKNOWLEDGMENTS

This work has been supported by LEFE and by ANR (project FLOWINg). The authors are grateful to Bach Lien Hua and Peter Bartello for stimulating discussions and useful suggestions. Christelle Bordas contributed at early stages of this work, which is gratefully acknowledged. The authors thank Stephen Griffiths and an anonymous reviewer for constructive comments which helped improve the manuscript.

Downloaded 14 Oct 2009 to 129.199.72.169. Redistribution subject to AIP license or copyright; see http://pof.aip.org/pof/copyright.jsp

[1]J. A. Knox, "Inertial instability," in *Encyclopedia of Atmospheric Sciences*, edited by J. R. Holton, J. A. Curry, and J. A. Pyle (Academic, London, 2003), pp. 1004–1013.
[2]D. A. Bennetts and B. J. Hoskins, "Conditional symmetric instability—A possible explanation for frontal rainbands," Q. J. R. Meteorol. Soc. **105**, 945 (1979).
[3]B. L. Hua, D. W. Moore, and S. Le Gentil, "Inertial nonlinear equilibration of equatorial flows," J. Fluid Mech. **331**, 345 (1997).
[4]T. J. Dunkerton, "On the inertial stability of the equatorial middle atmosphere," J. Atmos. Sci. **38**, 2354 (1981).
[5]J. P. F. Fortuin, H. M. Kelder, M. Sigmond, R. Oemraw, and C. R. Becker, "Inertial instability flow in the troposphere over Suriname during the South American Monsoon," Geophys. Res. Lett. **30**, 1482, doi:10.1029/2002GL016754 (2003).
[6]K. Sato and T. J. Dunkerton, "Layered structure associated with low potential vorticity near the tropopause seen in high-resolution radiosondes over Japan," J. Atmos. Sci. **59**, 2782 (2002).
[7]J. A. Knox and V. L. Harvey, "Global climatology of inertial instability and Rossby wave breaking in the stratosphere," J. Geophys. Res. **110**, D06108, doi:10.1029/2004JD005068 (2005).
[8]P. H. Stone, "On non-geostrophic baroclinic instability," J. Atmos. Sci. **23**, 390 (1966).
[9]T. J. Dunkerton, "A nonsymmetric equatorial inertial instability," J. Atmos. Sci. **40**, 807 (1983).
[10]D. E. Stevens and P. E. Ciesielski, "Inertial instability of horizontally sheared flow away from the equator," J. Atmos. Sci. **43**, 2845 (1986).
[11]S. D. Griffiths, "The limiting form of inertial instability in geophysical flows," J. Fluid Mech. **605**, 115 (2008).
[12]T. J. Dunkerton, "Inertial instability of nonparallel flow on an equatorial β plane," J. Atmos. Sci. **50**, 2744 (1993).
[13]P. D. Clark and P. H. Haynes, "Inertial instability on an asymmetric low-latitude flow," Q. J. R. Meteorol. Soc. **122**, 151 (1996).
[14]M. D'Orgeville and B. L. Hua, "Equatorial inertial-parametric instability of zonally symmetric oscillating shear flows," J. Fluid Mech. **531**, 261 (2005).
[15]S. Griffiths, "The nonlinear evolution of zonally symmetric equatorial inertial instability," J. Fluid Mech. **474**, 245 (2003).
[16]S. Griffiths, "Nonlinear vertical scale selection in equatorial inertial instability," J. Atmos. Sci. **60**, 977 (2003).
[17]J. R. Taylor and R. Ferrari, "On the equilibration of a symmetrically unstable front via a secondary shear instability," J. Fluid Mech. **622**, 103 (2009).
[18]C. Y. Shen and T. E. Evans, "Inertial instability of large Rossby number horizontal shear flows in a thin homogeneous layer," Dyn. Atmos. Oceans **26**, 185 (1998).
[19]R. C. Kloosterziel, G. F. Carnevale, and P. Orlandi, "Inertial instability in rotating and stratified fluids: Barotropic vortices," J. Fluid Mech. **583**, 379 (2007).
[20]R. C. Kloosterziel, P. Orlandi, and G. F. Carnevale, "Saturation of inertial instability in rotating planar shear flows," J. Fluid Mech. **583**, 413 (2007).
[21]C. G. Rossby, "On the mutual adjustment of pressure and velocity distributions in certain simple current systems II," J. Mar. Res. **1**, 239 (1938).
[22]R. Plougonven and V. Zeitlin, "Lagrangian approach to the geostrophic adjustment of frontal anomalies in a stratified fluid," Geophys. Astrophys. Fluid Dyn. **99**, 101 (2005).
[23]A. J. Thorpe and R. Rotunno, "Nonlinear aspects of inertial instability," J. Atmos. Sci. **46**, 1285 (1989).
[24]B. J. Hoskins and F. P. Bretherton, "Atmospheric frontogenesis models: Mathematical formulation and solution," J. Atmos. Sci. **29**, 11 (1972).
[25]L. Landau and E. Lifchitz, *Mécanique des Fluides*, 2nd ed. (Editions Mir, Moscow, 1989).
[26]M. Abramowitz and I. Stegun, *Handbook of Mathematical Functions*, Applied Mathematics Series (National Bureau of Standards, Washington, DC, 1964).
[27]E. Kunze, "Near-inertial wave propagation in geostrophic shear," J. Phys. Oceanogr. **15**, 544 (1985).
[28]R. C. Kloosterziel and G. F. Carnevale, "Vertical scale selection in inertial instability," J. Fluid Mech. **594**, 249 (2008).
[29]S. D. Griffiths, "Weakly diffusive scale selection for the inertial instability of an arbitrary shear flow," J. Fluid Mech. **594**, 265 (2008).
[30]W. C. Skamarock, J. B. Klemp, J. Dudhia, D. O. Gill, D. M. Barker, W. Wang, and J. G. Powers, "A description of the Advanced Research WRF Version 2," NCAR technical note, 2005 (can be downloaded freely from http://www.mmm.ucar.edu/wrf/users/docs/arw_v2.pdf).
[31]W. Blumen and R. Wu, "Geostrophic adjustment: Frontogenesis and energy conversion," J. Phys. Oceanogr. **25**, 428 (1995).
[32]R. Wu and W. Blumen, "Geostrophic adjustment of a zero potential vorticity flow initiated by a mass imbalance," J. Phys. Oceanogr. **25**, 439 (1995).
[33]M. V. Kalashnik, "Forming of frontal zones during geostrophic adjustment in a continuously stratified fluid," Izv., Atmos. Ocean. Phys. **34**, 785 (1998).
[34]M. V. Kalashnik, "Geostrophic adjustment and frontogenesis in a continuously stratified fluid," Izv., Atmos. Ocean. Phys. **36**, 386 (2000).
[35]W. Blumen, "Geostrophic adjustment," Rev. Geophys. Space Phys. **10**, 485, doi:10.1029/RG010i002p00485 (1972).
[36]E. Scherer and V. Zeitlin, "Instability of coupled geostrophic density fronts and its nonlinear evolution," J. Fluid Mech. **613**, 309 (2008).
[37]P. Billant and J. M. Chomaz, "Theoretical analysis of the zigzag instability of a columnar vortex pair in a strongly stratified fluid," J. Fluid Mech. **419**, 29 (2000).
[38]V. Zeitlin, "Decoupling of balanced and unbalanced motions and inertia-gravity wave emission: Small versus large Rossby numbers," J. Atmos. Sci. **65**, 3528 (2008).
[39]C. Dong, J. C. McWilliams, and A. F. Shchepetkin, "Island wakes in deep water," J. Phys. Oceanogr. **37**, 962 (2007).

Downloaded 14 Oct 2009 to 129.199.72.169. Redistribution subject to AIP license or copyright; see http://pof.aip.org/pof/copyright.jsp